

MOLECULAR DYNAMICS SIMULATIONS OF DISLOCATIONS MULTIPLICATION AND INTERACTIONS CLOSE TO ROUGH SURFACES

BY

Javier Antonio Gonzalez Joa

DISSERTATION

Submitted in partial fulfillment of the requirements

For the degree of Master of Nanoscience and Nanotechnology

In the Graduate Program of Nanoscale Engineering of the

Université de Lyon

September 4, 2018

Work performed at : Laboratoire MATEIS, INSA-LYON, Univ-Lyon 1, CNRS, UMR5510

Under the supervision of : Dr. Jonathan Amodeo

| | | |
|-------------|--|-----------|
| I. | Introduction | 1 |
| II. | Methods | 6 |
| | 2.1 Molecular dynamics simulations and tools | 6 |
| | 2.2 Methodology to generate samples with random surfaces | 8 |
| | 2.3 Deformation and FR source | 13 |
| | 2.4 Simulation setup | 15 |
| III. | Results | 17 |
| | 3.1 Surface equilibration | 17 |
| | 3.2 Tensile tests | 18 |
| IV. | Conclusion | 27 |
| | References | 28 |

I. INTRODUCTION

When evaluating physical properties of solid materials, surfaces play a crucial role as for example in catalysis [1], wetting process [2] or in the field of mechanics. For example, in microstructured Ti ($\alpha+\beta$) alloys [3]; it has been shown how the yield stress and the ductility are improved in function of the α size. Also it has been reported experimentally an increase in the hardness when reducing the surface roughness of boron carbon nitride coatings synthesized by ion beam assisted deposition [4]. Another example is about conductors that may lose their electrical properties if their contact area surfaces are not perfectly flat or well-polished [5]. In the same way, the optical properties may change depending on the surface contact state. For instance, it has been reported the influence of nanotextured contacts presents on amorphous silicon solar cells in the light trapping and plasmonic losses [6].

In experimental sciences, the surface of the sample is investigated to provide information about its composition and properties. Between the methods used to characterize them we can mention the Atomic force microscopy (AFM) [4], Scanning electron microscopy (SEM), XPS and AES. Most of them may be done in ultra-high vacuum (UHV) with a non-trivial sample preparation.

Recently an experimental UHV AFM/STM for studies of nanostructures was developed at Poitiers institute by the group of Christophe Coupeau [7]. It constitutes the basement of the program NANOPLAST aimed to study surface of micro and nano-objects under strain/stress test at different temperature [7]. In a first study they reported the interaction of slip trace with a vicinal step at different temperature in gold samples [8]. They propose a model describing the interaction between the trace and the vicinal taking into account surface energy considerations.

.Recently the in situ AFM/STM device developed at the NANOPLAST team has been used to investigate dislocation traces at the surface of Ni_3Al . Ni_3Al is a very complex intermetallic material with plastic deformation governed by super dislocation in different slip modes (cubic and orthogonal) [9]. Imaging both surface and bulk dislocation glide is crucial for the understanding of the mechanical properties. They observed the stop of a dislocation emerging at the surface at the surface when interacting with a surface step (Figure 1.1).

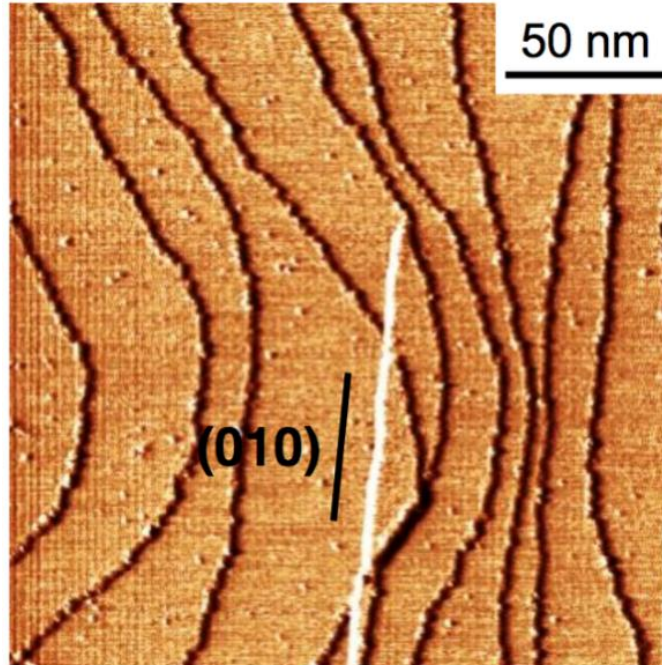


Figure 1.1: Dislocation stopped by the one-layer step at the surface of Ni_3Al . Image courtesy of Christophe Coupeau, from Poitiers institute.

Using numerical simulations to study mechanical properties of material may bring some advantages over experimental sciences. The chemical or mechanical preparation of sample can be sometimes hard, expensive and time consuming process. In the case of mechanical studies, the investigation of the propagation of dislocations inside a sample during a compressional test is usually done by in situ TEM, which allows (with some limitations) to see the propagation of dislocation inside the material. With Molecular Dynamics (MD) simulations, the observation and study of dislocation is easier. Several processing and post processing softwares allows for a better identification and classification of the different structure and physical properties when a simulation is performed. Using numerical approaches in general constitute an interested alternative to the tough experimental process. In the case of MD the studies of dislocation is done considering the samples made of perfectly flat surfaces. However, in experimental sciences; by using SEM or TEM microscopy techniques is possible to identify sections in a sample with not perfectly planar geometries. In this study we will investigate how to generate roughness at the atomic scale and shows how rough surface can influence dislocation mobility trying to explain observation presented in Figure 1.1. This model will be applied to copper, a model faced centered cubic (FCC) metal.

Theoretical approaches of surface are attached to the field of friction mechanics or adhesion. For example Lars Pastewka and Mark O. Robbins [10] used the Fourier-filtering algorithm and the Hurst exponent to characterize roughness in simulations of adhesive contact between rough surfaces for a wide range of adhesion strength, surface geometries, and material properties [11].

Several models for generations of random surface (RS) are reported in the literature (linear transformation, time series, Fourier filters, etc.). Patir [12] proposes a linear transformation method to generate parameterized three-dimensional rough surfaces using autocorrelation functions and a random number generator. With it, the RS will have a coherent modulation of the surface. This methodology conduces to a system of nonlinear equations with the autocorrelation coefficients to be determined. Mostly it can be solved by using an iterative method (e.g. Newton-Raphson) to find the autocorrelation coefficients.

Although the linear transformation method is a simple way to obtain random rough surfaces, it depends on an iterative method with doubtful convergence conditions. An improvement of this methodology was proposed by Hu et al. [13], where the discrete Fourier transform is used. With this, a simplification is introduced and the height distribution can be expressed in terms of their spectral components. Now, determining the autocorrelation coefficients is simpler and is equivalent to apply a digital filter constraining the expected frequency response.

One of the conclusions reported by Hu is that this methodology constitutes an extension of the linear transformation method and is mathematically identical to the time series model proposed by Watson et al. [14]. This model avoids the non-linear system of equations used in Patir's method by introducing a change of domain. The coefficients to determine will have a non-trivial expression if the filter proposed is not linear and perfectly symmetric which will affect the roughness of the surface.

In the other hand, when study realistic samples not only the shape or the surface structure are the parameters to take into account. When a tensile or compressional test is performed beyond the elastic limit; plastic deformation takes place and this process is characterized by dislocations moving within the crystal structure.

The process of dislocation multiplication inside atomic samples is highly dependent of the orientation of the gliding plane and the conditions of the stress applied. For instance, a dislocation may propagate or not depending if the stress is enough and if it is applied in the correct direction. Slip is more favorable to occur in close packed planes due to energetic considerations.

Close packed planes have the higher atomic density, it means that the effort required to move dislocations in this plane is comparatively small. For the point of view of natural process, they tend to occur with a minimum of energy, in the case of dislocations this energy is directly proportional to the square of the Burgers vector, and at the time, it is smaller in the close packed plane. Defining the number of close packed planes and the possible direction of slip leads to the numbers of slip systems present in the material.

Cooper presents FCC crystal structures and there are twelve slip systems. Four slip planes $\{111\}$ with three slip directions $\langle 110 \rangle$ for each slip plane. Burger vector lies in the slip plane and are used to characterize dislocations; with it the magnitude and direction of slip are completely defined. In FCC crystals the dislocations move in the $\{111\}$ set of planes, in the $\langle 110 \rangle$ direction and with $a/2[110]$ Burgers vector.

Dislocations can be classified on screw, edge or mixed. Most dislocations found in crystals are probably neither pure edge nor screw but mixed. The character of a dislocation is expressed by its Burgers vector. In the case that the Burgers vector is perpendicular or parallel to the dislocation line; the dislocation is called “edge” or “screw” respectively. Even when a mixed dislocation has portions of edge and screw dislocation within the dislocation loop, the Burgers vector remains the same.

A particular characteristic of screw dislocation in FCC materials is that they can switch from one {111} plane to other. This process is known as cross-slip and can occur more than once (double cross-slip, etc.).

In studies of dislocation multiplications one of the most accepted model is the Frank-Read (FR) source. This kind of dislocation can be seen as dislocation segment between two fixed points (Figure 1.2a). In the classical mechanism for dislocation multiplication when the stress applied overcome a critical value the dislocations start to bend creating dislocation loops. One of the characteristics of these dislocations loops is that they carried the same Burger vector as the original dislocation segment

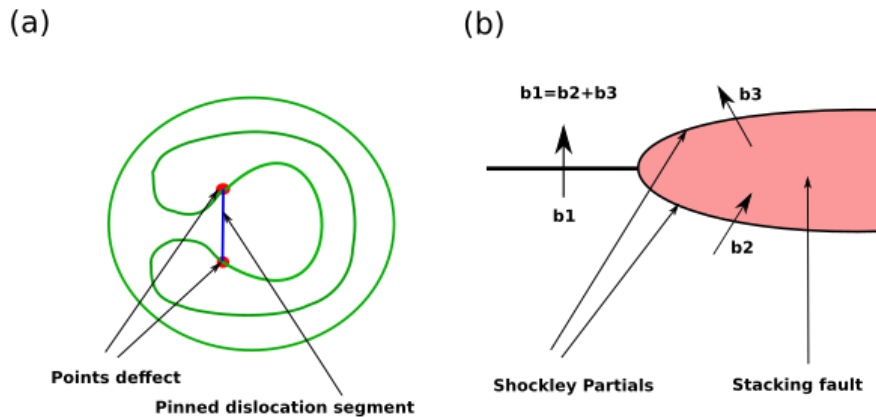


Figure 1.2: (a) Graphical representation of a FR source. A dislocation line is pinned at two immobile pinning points. When stress is applied the dislocation bends and propagates forming a dislocation loops. (b) Dislocation dissociation into two Shockley partials.

Dislocation dissociation (Figure 1.2b) occurs when the strength of dislocation is more than unity. The system becomes unstable and dissociate into two dislocations (Shockley partials) with the stacking fault between them. The dissociation reaction $b_1 = b_2 + b_3$ will occur when $b_1^2 > b_2^2 + b_3^2$.

We attempt with this work to understand the possible interaction taking place in dislocation multiplication when interacting with roughness at the samples surfaces. With this aim we will develop a methodology to introduce roughness in a perfectly flat molecular dynamic sample by intercepting it with a pre-generated random surface based in the theory for random surfaces proposed by Sjodin [15]. Then a FR dislocation will be introduced considering the method of de Koning [16]. Finally the interaction between the roughness and the mobility of the dislocation will be studied performing simulations of tensional test over the sample.

This work is organized in the following way:

In the next section, we will shortly introduce the theory used to perform MD simulations. Then the methodology of Sjodin [15] to generate random surface and the adaptation to atomistic samples is described. It will be followed by the basics of FR dislocation theory and plasticity to end up with the discussion of the simulation strategy.

Then the results section starts with the surface equilibration analysis to make the surface energetically more stable. Tensile simulation is presented starting by discussing the stress-strain curve. The effect of the roughness over the velocity of the dislocation is discussed.

II. METHOD

In this chapter the main concepts of MD will be shortly introduced. A complete description on of how to generate MD samples with RS is presented followed by the introduction of FR sources and the basic equation of plasticity.

2.1 Molecular dynamics simulations and tools

We used MD to study the evolution of the dislocation inside the sample and the interaction with the surface. Working at atomic scale the sample is modeled not like a continuum medium but as a discrete three-dimensional distribution of atoms interacting between them and with the external perturbations applied. Physically; it is a mechanical “many body” problem where the equation of motion must be solved. The computation is done using LAMMPS [17]; professional software for molecular dynamic whose name is acronyms of Large-scale Atomic/Molecular Massively Parallel Simulator developed at Sandia National Laboratories.

The core of the calculation performed by LAMMPS lies in the interatomic potential declared to be taken into account while solving Newton second law:

$$\frac{d^2 r_i(t)}{dt^2} = \frac{1}{m_i} F_i(t) \quad (2.1)$$

Where r_i , m_i and F_i represent the position, mass and force of particle i respectively. The interaction potential $V(r_i)$ and the force are related by

$$F_i = -\nabla V(r_i) \quad (2.2)$$

The kind of interaction between the atoms taking place in a sample is very broad. For instance, the interaction depends of kind of bonding, electronic distribution etc. Depending of the nature of the problem to be solved, the potential may be expressed in very simple contributions like a columbic term or Lennard-Jones, or even more complicated. Usually the potential used depend strongly of the material to be modeled. In our case of modeling metals, we use the embedded atom method (EAM) from Mishin et al. [18] that apply for Cu. The total energy of an atom (E_i) is:

$$E_i = \frac{1}{2} \sum_{j \neq i} \varphi_{\alpha\beta} + F_{\alpha} \left(\sum_{j \neq i} \rho_{\beta}(r_{ij}) \right) \quad (2.3)$$

Where the embedding energy F_α is a function of the atomic density ρ . φ is the pair potential interaction. The types of elements are represented by α and β . The summation must be evaluated over the number of neighbors j of the element i inside the cutoff distance.

Since we are modeling object of the nanoscale the physical parameters used to characterize them still in the bulk domain. The connection with the “macro-world” is well understood and obeys the laws of statistical mechanic. Different ensembles and different thermostat/barostat are used in the control of the distinct parts of the evolution of the model.

For a system containing N atoms of the same mass that interacts by a potential V the total energy can be express by its Hamiltonian as:

$$H(\{r_i, p_i\}) = \sum_{i=1}^N \frac{|p_i|^2}{2m} + V(r_i) \quad (2.4)$$

With p_i the momentum of the particle i , and considering the Hamilton equations:

$$\frac{dr_i}{dt} = \frac{\partial H}{\partial p_i} \quad (2.5)$$

$$\frac{dp_i}{dt} = -\frac{\partial H}{\partial r_i} \quad (2.6)$$

The final equation of motion to be solved can be written as:

$$m \frac{d^2 r_i}{dt^2} = -\frac{\partial V(r_j)}{\partial r_i} \quad (2.7)$$

The use of Hamiltonian mechanic allows for a simplest solution for calculating the position and velocity (momentum) of the particles. In MD, several algorithms are used to solve the differential equations. LAMMPS uses the velocity Verlet algorithm which consists on a finite difference approximation of the acceleration (equation 2.8). With the initial condition been the r_i at $t=0$, the Verlet algorithm will compute the atomic position at any $t + \Delta t$.

$$a_i(t) = [r_i(t + \Delta t) - 2r_i(t) + r_i(t - \Delta t)]/(\Delta t)^2 \quad (2.8)$$

From equation (2.8) can be obtained an expression for the position at any time. In this way the velocity can be estimated by a simple calculation of the atoms position with dependence of time. Several modifications to the Verlet algorithm were introduced to increase precision. One of the most popular and used in LAMMPS is the velocity Verlet algorithm.

Like many others open source softwares for numerical modeling the methodology of working of LAMMPS is mostly divided in three parts. First, the pre-processing; i.e the geometrical construction of the sample is done here with AtomsK [19] and a home-made software. Although LAMMPS is fully capable to design the sample geometry; the use of AtomsK is more direct, robust and simple. Then, the scripting part, which contains the core of the numerical experiment. And finally the post process, where the analysis of the results is done.

Special attention should be taken in the definition of the nature of the boundary conditions (BC), most of the time, periodic BC are used in MD. But also, rigid or free BC can be implemented. In our case, the strategy for modeling samples with RS implies a correct selection of the BC and deformation method. Due to the nature of the calculation of stress and pressure in LAMMPS, the direction of the deformation, the boundaries and stress tensor may lead to some problems and errors in the model. The methodology chose will be explained in detail in the next sections.

After the simulation, the visualization of the sample and the control of the thermodynamics outputs are done by using Ovito [20] and MatLab.

2.2 Methodology to generate samples with random surfaces

Attending to its composition a model for RS may be consider as isotropic or anisotropic depending if its properties changes with a change in orientation. Mathematically; the roughness can be classified attending to its height distribution as random or not-random. In the case of presence of randomness; it may be useful to identify its distribution. For that the Gaussian classification may be taken into account. Finally, the complete description must include the autocorrelation classification. A more detailed description can be found in Figure 2.1

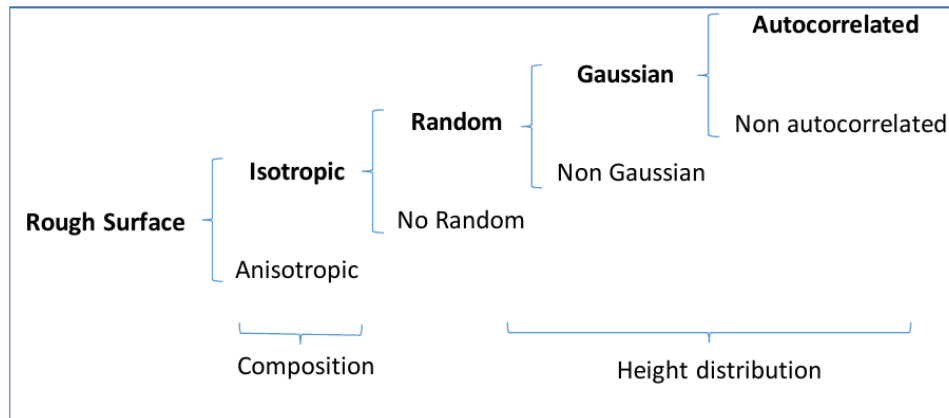


Figure 2.1. Representation of RS classification. The surface is classified by its composition and height. The classification of the RS used in this work is presented marked in dark black color.

In this work, a method adapted from the work of Sjodin [15] will be used. Random surfaces can be described using two main constituents i.e. a random number generator and a periodic expression. Usually, a periodic function has the form of a cosine (or a sine). 2D rough surfaces can be obtained as the superposition of elementary periodic functions:

$$z = \sum_{m=0}^M \sum_{n=0}^N A * \cos(2\pi(mx + ny) + \varphi) \quad (2.9)$$

A is the amplitude and φ the phase of the function. Inside the cosine function of equation (2.9), the wavenumbers m and n induce a gradual change in the spatial frequency. For generating random surfaces it is necessary to perturb the phase and amplitude component in a non-deterministic way. The amplitude can be set as a matrix of Gaussian distributed random numbers with specified mean and standard deviation (A_{mn}). However, in order to obtain more mathematical control over the roughness surface two more contributions to equation (2.9) should be made: (i) the phase angle φ can take any value in the interval $[-\pi/2, \pi/2]$ with the same probability, (ii) mathematically, frequency and amplitude are correlated. Therefore a more rigorous expression of A_{mn} is proposed by Sjodin [15]:

$$fc = (m^2 + n^2)^{-b/2} \quad (2.10)$$

This equation is multiplied by the matrix of Gaussian distributed random numbers A_{mn} . Now, b represents a spectral exponent and it will parameterize how fast the high frequencies are attenuated. Putting all together; a final expression for the desired random surface can be written as

$$z = C1 * \sum_{n=-N}^N \sum_{m=-M}^M fc * G(n, m) * \cos(2\pi(mx + ny) + U(n, m)) \quad (2.11)$$

Where $G(n, m)$ and $U(n, m)$ are the matrix array of normal or Gaussian distributed and Uniform distributed random numbers. $C1$ is a normalization factor. x and y are the cartesian coordinates. Equation (2.11) will be periodic in the interval $y \in \{0, 1\}$. It can be avoided by taking values inside or outside of that boundary. The fact that m and n can be positive or negative makes the surface to be generated with no preferred oscillation direction. The spatial frequency is controlled by the maximum number that n or m can reach. It means; if n and m can go until maximum values N or M then the shortest wavelength in x and y direction will be in the order of $\lambda_x = 1/N$ and $\lambda_y = 1/M$. Euler relationship implies that equation (2.11) can be seen as a discrete cosine transform or discrete Fourier transform when just the real part is considered. A more detailed description in the previous methodology of obtaining equation (2.11) can be found in [15]. There is also an explanation of

extrapolation of this method for developing the randomized closed curves and cylinders. Figure 2.2 shows an example of four rough surfaces generated with different spectral exponents.

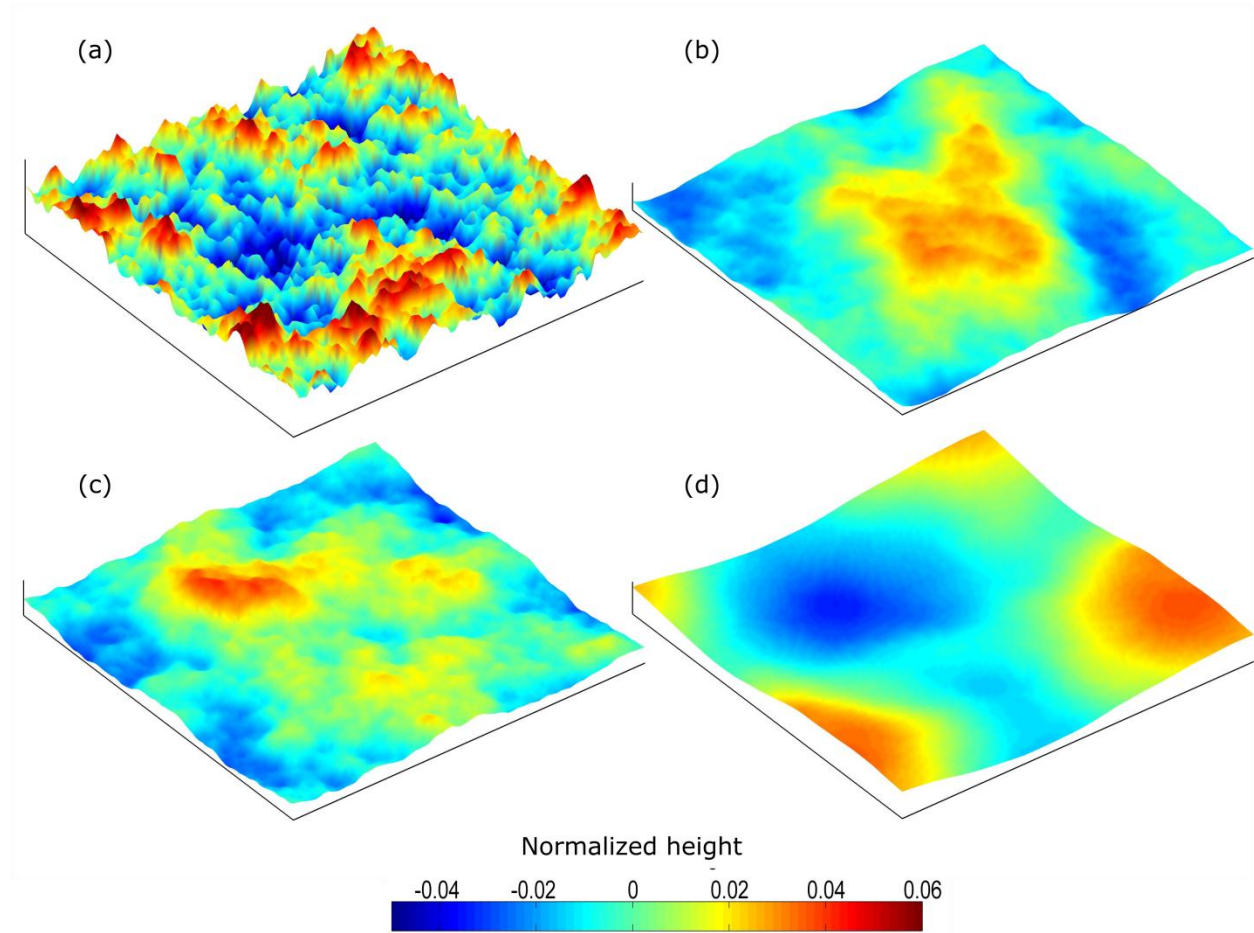


Figure 2.2: Influence of the expectral exponent b on the roughness of modeled surface considering $N = M = 30$ and $C1=0.01$. (a) $b = 1.2$; (b) $b = 1.8$; (c) $b = 2.2$; (d) $b = 2.8$. The Cartesian coordinates in the figure are normalized.

The roughness is associated with the variation of height with respect to a central line. In the case of an experimental surface, a mathematical expression for autocorrelation should be given. This is not necessary for modeling random surface since the correlation length is known a priori. Different statistical parameters (mean, RMS , skewness and kurtosis) are used to characterize the roughness of the surface [21-23]. If the final height for random surface follows a Gaussian distribution the standard deviation (σ) represents the main parameter for such characterization. If the final height is not normally distributed other parameters should be considered. We start defining the mean line value:

$$l = \frac{1}{N.M} \sum_{i=1}^{N.M} z_i \quad (2.12)$$

Based on equation 2.12 we can calculate σ and the *RMS* like

$$\sigma = \sqrt{\frac{1}{N.M} \sum_{i=1}^{N.M} (z_i - l)^2} \quad (2.13)$$

$$RMS = \sqrt{\frac{1}{N.M} \sum_{i=1}^{N.M} z_i^2} \quad (2.14)$$

If the mean line value is strictly zero the values of σ and *RMS* will match. These two parameters should be enough to characterize the roughness of any surface but they do not give any information about the final distribution (Figure 2.3a). For a complete mathematical description we use skewness (*sk*) and kurtosis (*K*) (Figure 2.3b) as defined by equation (2.15) and (2.16)

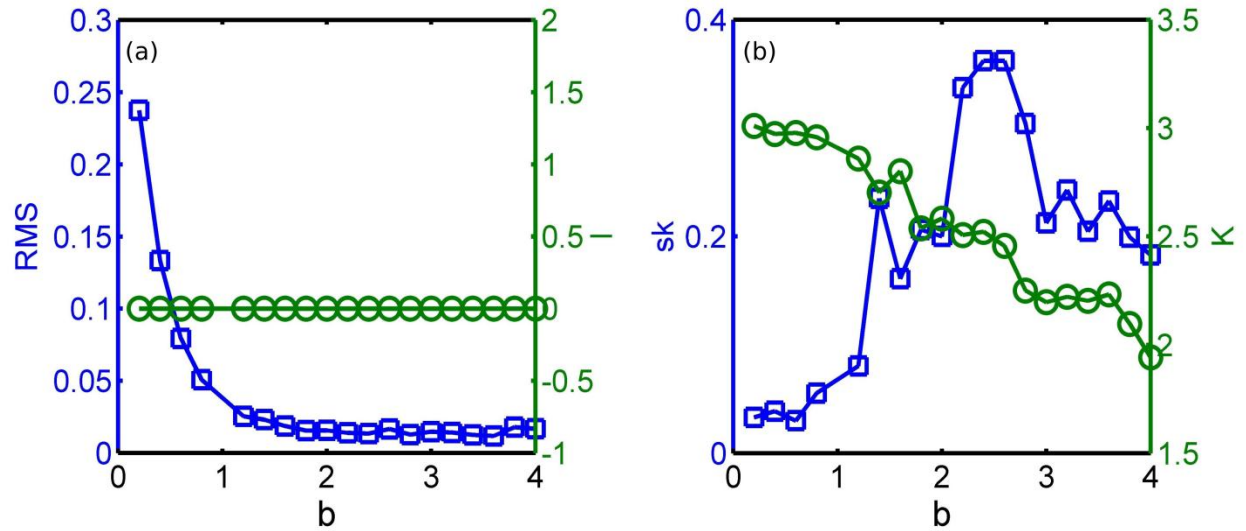


Figure 2.3: Statistical study of spectral exponent b . In blue and green respectively the *RMS* and mean central line (a); in the same way the *sk* and *K* are shown in (b).

$$sk = \frac{1}{\sigma^3 \cdot N.M} \sum_{i=1}^{N.M} (z_i - l)^3 \quad (2.15)$$

$$K = \frac{1}{\sigma^4 \cdot N \cdot M} \sum_{i=1}^{N \cdot M} (z_i - l)^4 \quad (2.16)$$

The parameter K and sk characterize the shape form of any data. The sk measures the lack of symmetry in the distribution shape while K characterizes the degree of flatness with $sk = 0$ and $K = 3$ in the case of normally distributed data.

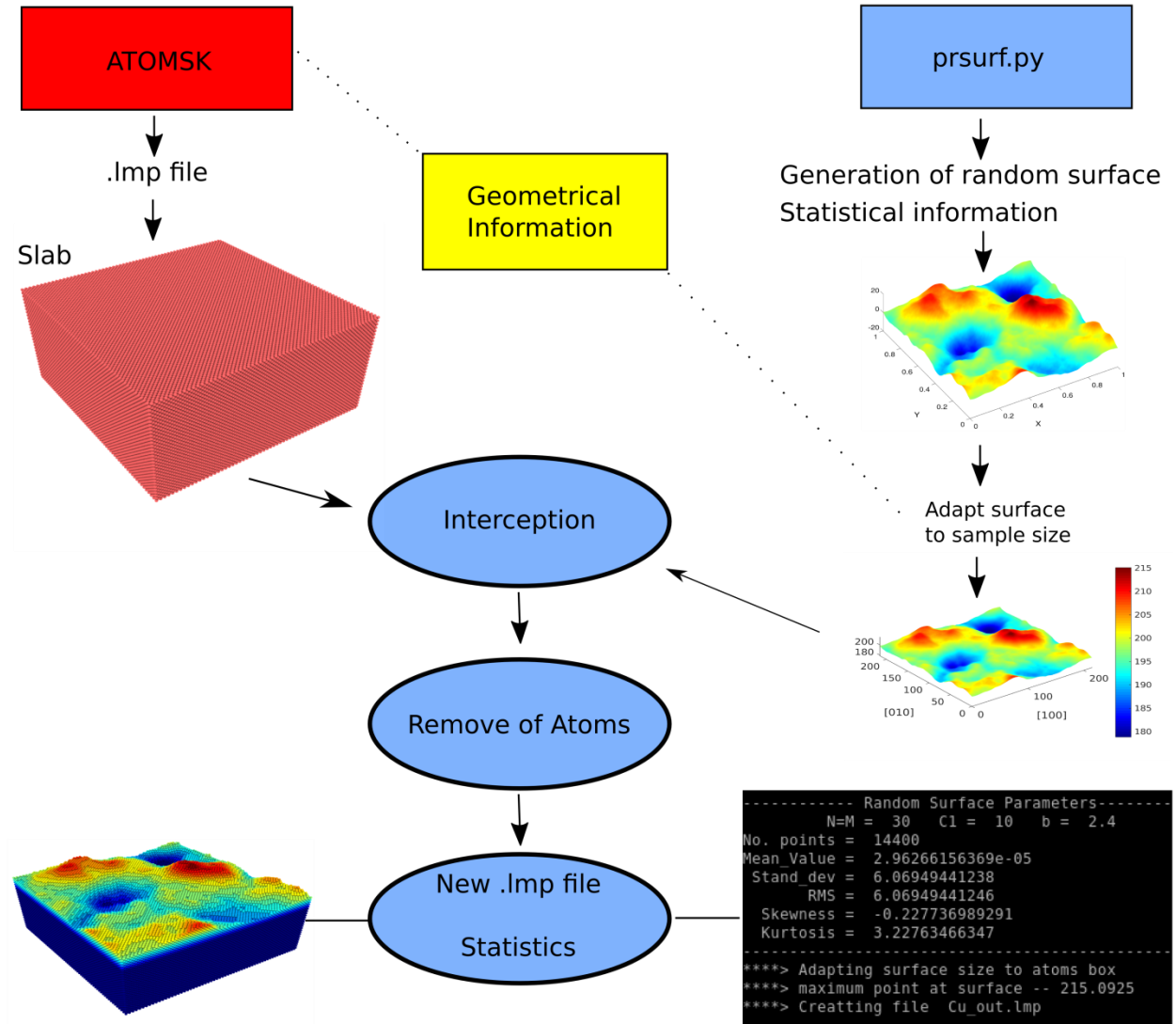


Figure2.4: Diagram illustrating the MD sample fabrication. The first step is to create an MD sample by using AtomsK while in parallel a RS is created. The software will determine the size and position distribution of atoms to create the mesh grid for the sample. The steps followed are as showed following the arrows in the right part of the diagram.

The equation (2.11) was implemented in a (Python) code. The code is capable to generate outputs files with the cartesian coordinates of the RS, perform its statistical characterization (σ , RMS ..etc) and generate an atomistic sample (in LAMMPS compatible format) with the surface shaped by the pre-generated RS.

When the output desired is a RS the process is straight forward. Once the parameters (b , N , M , and $C1$) are setup inside the code script the surface will be generated taking into account the desire geometry (plane, cylinder or sphere). The planar RS will be generated normalized (with x and y axis between 0 and 1) and with a density of points of 100 points per axis.

In the case of generate an atomistic sample with RS, the first step is to generate an atoms file (LAMMPS compatible format) of the desired size by using Atomks. Then, produce the shape of the random surface in the top layers of the XY plane by numerical interception between the Atomsk generated sample and the RS. The code will read the atomistic sample and determine the distribution of point in x and y direction. Then this distribution of points will be taken into account during the generation of the normalized random surface. Before the interception, the surface is adapted to the real size of the XY plane and the maximum height in the surface is matched with the maximum Z value of the atomistic sample. Finally, an algorithm detects the numbers of layers that will be involved in the interception process and a point by point comparison between the sample and the surface is performed. The atoms lying over the surface are removed and a new file with the new configuration is exported. At the end of the process the code reports the statistical analysis of the random surface, the number of atoms removed, the new file produced and the time consumed during the process.

One of the advantage of using this methodology for RS generation is the possibility of obtain periodic surfaces in X and Y axis. It allows the use of coordinate transformations (spherical, cylindrical, etc.) for obtain symmetric 3D object with RS that can be used for MD, but also for FEM simulations (Figure 2.5).

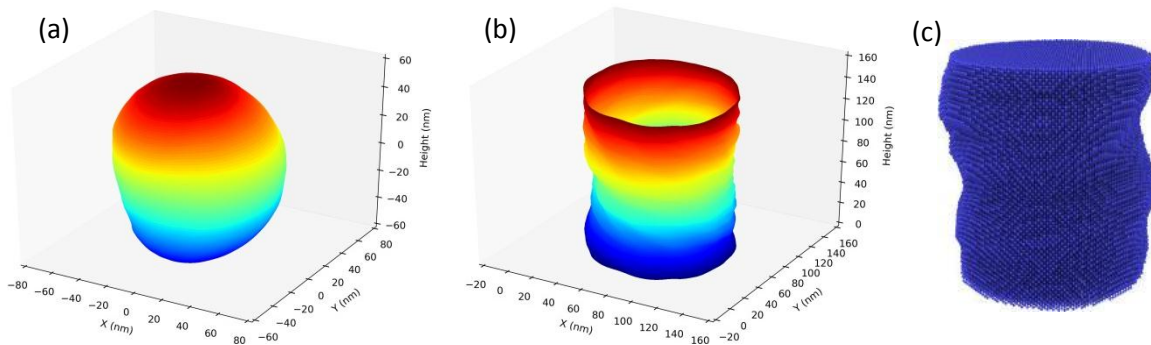


Figure 2.5: Three dimensional rough and symmetric objects shaped by random surfaces. (a) Sphere, (b) Cylinder, (c) nanowire section designed for MD simulations.

2.3 Deformation and FR source

In experiments and MD simulations, when a material is deformed elastically (without dislocation glide), the first stage of deformation follows the Hook's law.

$$\sigma = E\epsilon \quad (2.17)$$

Where σ and ϵ represent the stress and strain respectively. σ takes units of pressure $\sigma = F/A$ while $\epsilon = \frac{L}{L_0} - 1$ is adimensional. The young modulus E is an intrinsic characteristic of the material and can be calculated by the slope of the stress-strain curve.

Then, plastic deformation happens. Here, to avoid unrealistic stress induced by dislocation nucleation from the surface, we used an algorithm developed by Y. Evan (PFE, GNL, INSA-LYON, 2016) to introduce pre-existing dislocation inside the sample. FR source can be created by removing a loop of rectangular shape made of two layers atoms from one of the $\{110\}$ planes (Figure 2.6a) with sides along $\langle 110 \rangle$ and $\langle 112 \rangle$ directions [16]. After a conjugate-gradient minimization process, two perfect edge dislocations dipoles are created with $\frac{1}{2} \langle 110 \rangle$ burger vectors gliding in $\{111\}$ planes (Figure 2.6b). These two mobile segments will dissociate after into pairs of Shockley partials (Figure 2.6c) dislocations when the stress is applied in an optimal direction

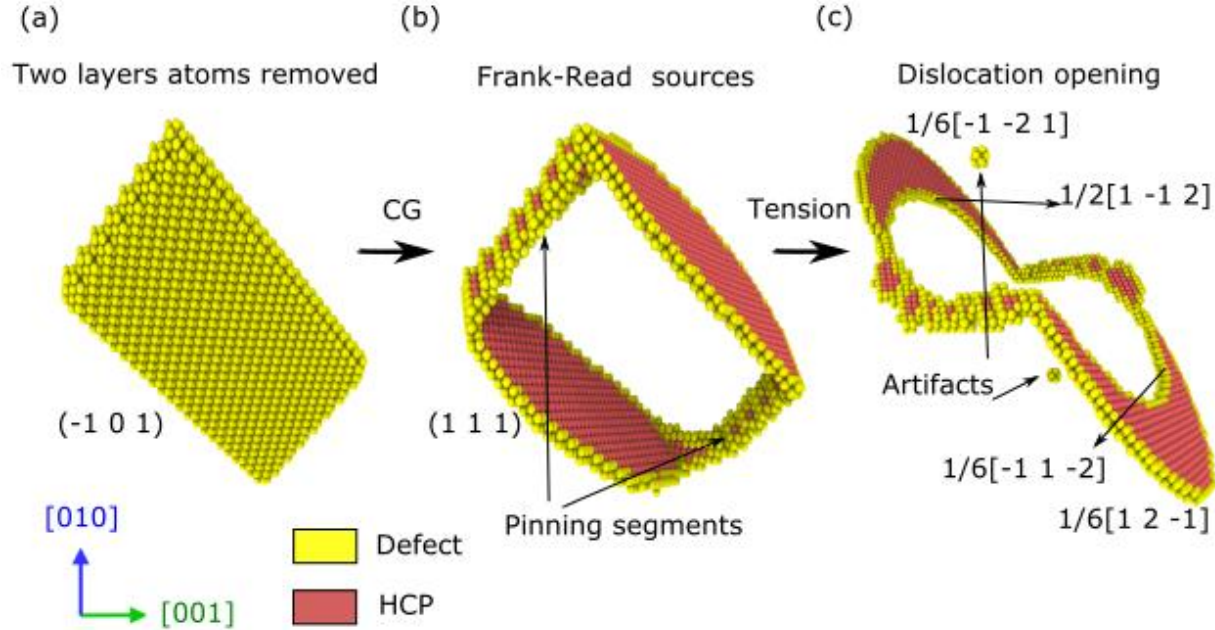


Figure 2.6: Creation of a FR source following the process described in de Koning et al [16]. Perfect crystals FCC atoms are removed for sake of clarity. “Defect” refers to defects atoms (dislocore, interface and other defective regions). (a) Removal of a two layer atoms in the (-101) plane. (b) FR dislocation type after CG minimization. (c) Dislocation opening with the stress applied.

During a test performed at constant (controlled) strain rate, the average dislocation velocity v and the shear rate $\dot{\gamma}$ are related by the Orowan equation:

$$\dot{\gamma} = \rho b v(\tau) \quad (2.18)$$

ρ is the mobile dislocation density, and b the burger vector.

Due to the pinning point of the FR source, the dislocation will multiply only under a critical shear stress needed to open the dislocation:

$$\tau_c = \frac{Gb}{L} \quad (2.19)$$

With G the shear modulus and L the distance between the two pinning points. Dislocation glide is driven by the shear stress on the glide plane, resolved in direction of b . At the time the critical resolved shear stress and the total stress applied to the system are linearly related by the Schmid law:

$$\tau = \sigma m \quad (2.20)$$

with m is the Schmid factor.

2.4 Simulation setup

Atomsk is used to create a Cu atomic file in two sizes with dimensions 361.5 or 506.1 Å in the three directions and oriented in the canonical system. The lattice parameter reported for Cu using EAM from Mishin et al. is 3.615 Å, which is the same value used in Atomsk to make the sample. Then a RS was generated with different $b = [2.0 \text{ 2.4 and 2.8}]$ $C1 = 10$ and $N = M = 30$ and adapted to the sample top surface. An important point to mention is that the roughening procedure does not impose any changes in the lattice parameter of the atoms in the surface. Two sizes of FR sources are tested, and they are produced introducing a rectangular hole made of two layers atoms with dimension 200 X 100 or 100 X 50 Å [16]. Only one FR source was introduced to avoid interaction between dislocations.

When using random surface for MD sample, special attention should be take when preparing the sample. For instance, using periodic boundary conditions (PBC) may lead to a complete loss of the RS morphology because of re-entering of atoms inside the simulation box. At the same time, not using PBC limit the ensemble to be used to assign and control temperature and pressure (the canonical (NVT) and Isothermal-Isobaric (NPT) ensembles cannot be used in LAMMPS if the BC are not periodic).

In order to avoid those incongruences, the simulation box is increased until five times the cut-off distance of the EAM potential at both Z-top and Z-bottom surfaces allowing to use PBC without any influence on the morphology of the RS.

Then, a three-step energy minimization was performed: first; a CG minimization, followed by the same scheme but allowing relaxation of the simulation box and finally Hessian-free truncated Newton algorithm (hftn). The CG minimization transforms the two layers hole mentioned previously into two FR

dislocation sources. Minimization does not ensure a hundred percent of certainty when determining the global minimum of the potential energy of the system. Thus, a thermal equilibration is used to ensure a correct relaxation of the surface of the sample. Temperature is introduced in the system starting at 50 K and allowed to relax using microcanonical (NVE) ensemble during 10 ps. Then, the temperature is increased up to 0.6 the melting temperature using NPT during 10 ps and kept constant during 50 ps. Finally, the temperature is decreased until its initial value during 10 ps. For this time-dependent process the time-step is fixed in 0.001 ps. The minimization process is completely time-independent; it means that Verlet algorithm only runs for the thermal equilibration at this stage.

With these conditions the tensile deformation is performed along x direction for three strain rates: 10^9 s^{-1} , 10^8 s^{-1} during the complete simulation and a strain rate variation starting at 10^9 s^{-1} during 30 ps to be then reduced to 10^8 s^{-1} . During the tensile test the temperature is kept constant at 25 K using the Nose-Hoover thermostat [24].

III. RESULTS

In this section, we discuss the effect of thermal equilibration on surface reconstruction. Then, tensile test simulations are presented. We detail how to reach optimum conditions for analysis of dislocation velocity and the effect of roughness on their mobility.

3.1 Surface equilibration

Before to study the deformation process, we have investigated the influence of temperature on the relaxation of the sample surface. This equilibration is performed in three steps: a first CG minimization, an equilibration at 0.6 melting temperature ($T_m=819$ K) and finally a last minimization. Thermodynamics variables evolutions during these steps are shown Figure 3.1.

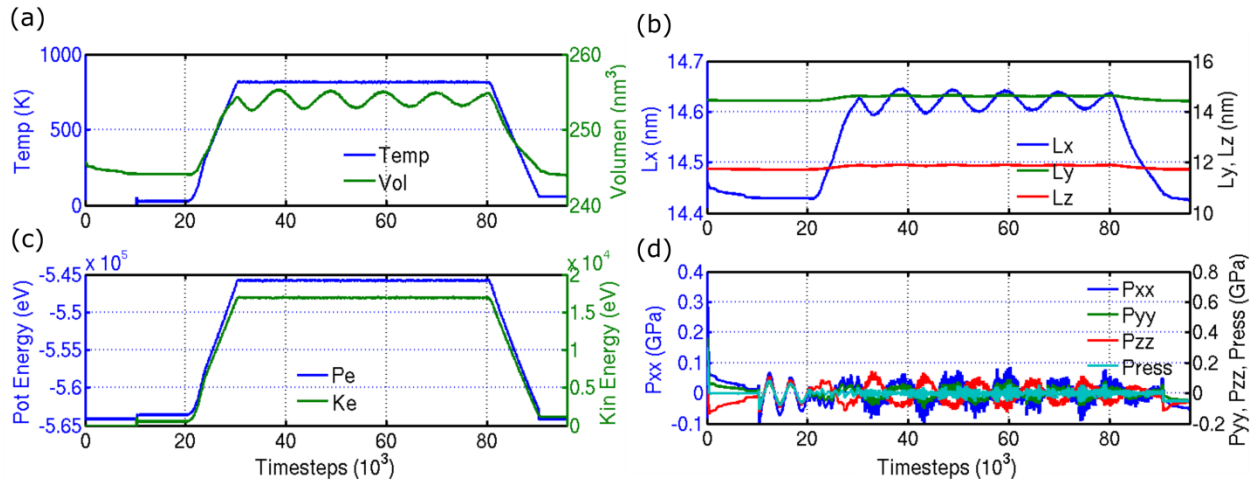


Figure 3.1: Thermodynamic control parameters during surface equilibration. (a) Temperature and Volumen vs time. (b) Dimension of the simulation box in the three direction vs time. (c) Potential and Kinetic energy vs time. (d) Pressure acting on the faces of the simulation box vs time (Press is the hydrostatic pressure of the system i.e., the trace of the stress tensor).

The temperature curve shows constant zero value during the first 10000 steps, what is observed also in the Kinetic energy. This is because the minimization process is temperature independent. After it, the temperature is kept constant during the followed 10 ps at 25 K to then be increase up to 819 K in 10 ps. This process is followed by a temperature equilibration at $0.6 \times T_m$ during 50 ps and a fast cooling step. The elongation in the three different directions as well as the evolution of the pressure and volume shows the expected thermal expansion-contraction caused by temperature variations. During this process the pressure maintains an oscillating behavior around zero.

An important point to notice is the reduction of the potential energy from -564123.36 eV to -564148.83 eV after the first and second minimization respectively. It means that after this process the sample is energetically more stable. In the following, before deformation; all the samples are submitted to the same thermal surface equilibration.

During minimization the atoms are slightly moved from their initial position when looking for a minimum value in the potential energy. This short distance does not change significantly the shape of the surface (the RMS keeps the same value of 0.04). Also, during the heating process the thermal vibration is increase and some atoms are allowed to be displaced to a new, more stable, position (Figure 3.2). Therefore, while the global shape of the surface is not affected by the high temperature equilibration process, local changes cannot be neglected.

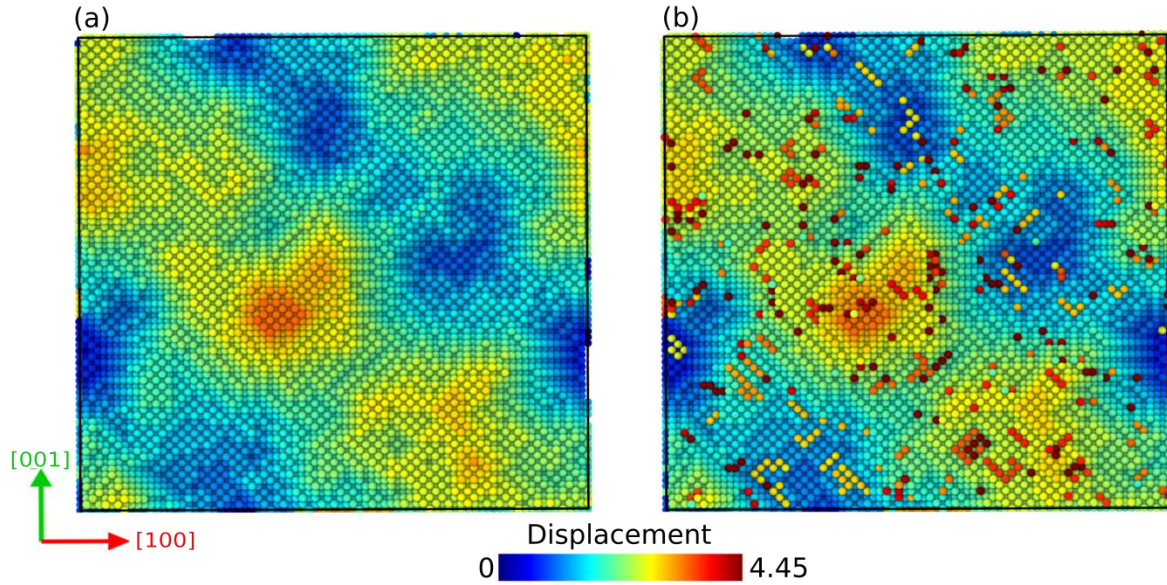


Figure 3.2: Displacement of atoms at the surface after 1st (a) and 2nd (b) minimization. The units of displacement vectors are in Å. The atomic displacement is computed relatively to the starting configuration, before any simulation.

In our case, the slight changes of the atomic arrangement at the surface (after the equilibration process) did not influence quantitatively the velocity of the emerging dislocation.

3.2 Tensile test

Tensile tests are performed for samples of different sizes, roughnesses (including a flat sample) and FR source size. Table 3.1 resumes the number of different cases studied and their denomination in function of the different parameters.

Merely, “Flat” refers to a sample without roughness and R_2.4 is a sample with roughness created with $b=2.4$. When the fractional number is followed by BFR it refers to the biggest of the FR sources deformed with the combination of the two strain rates. In the case the fractional numbers are followed by integers; it refers to the strain rate of the deformation. These samples are created with the smaller FR source size.

For the different samples tested, the evolution of the thermodynamic parameters is very similar. Figure 3.3 describes the case of the R_2.4 sample after the thermal equilibration. During the initial part corresponding to a minimization and equilibration stage at 25 K, the potential and kinetic energies are

kept at constant values. The box dimension L_x , L_y and L_z , is corroborated by the pressure and volume evolution up to 50000 steps. During this period the system is minimized allowing the box to change its dimensions (fix box relax command in LAMMPS), reason why the pressure and volume will oscillate until find equilibrium implying also a change in the box dimension.

Table 3.1: Parameterization of the different tensile tests performed. Several roughness (b), size of the FR source, sample size and strain rates are tested. In the denomination, “Flat” refers to the sample without roughness and “R” refers to rough samples. The rest of the parameters change by the variable influenced (BFR is Big FR referring to the dislocation source and BZ means big size referring to the largest sample size). Then, the following integer numbers refers to the power value in the strain rate (e.g. 9 for 10^9 /s strain rate) and the fractional to the roughness parameter b . The samples without integers numbers are deformed with the two strain rate combinations as described before.

| Sample | b | FR size | Sample size | Strain rate |
|------------|-----|-----------|-----------------------|---|
| Flat | - | 100 X 50 | 361.5 X 361.5 X 361.5 | $10^8 \text{ s}^{-1} / 10^9 \text{ s}^{-1}$ |
| R_2.4 | 2.4 | 100 X 50 | 361.5 X 361.5 X 361.5 | $10^8 \text{ s}^{-1} / 10^9 \text{ s}^{-1}$ |
| R_2.8 | 2.8 | 100 X 50 | 361.5 X 361.5 X 361.5 | $10^8 \text{ s}^{-1} / 10^9 \text{ s}^{-1}$ |
| R_2.4_BFR | 2.4 | 200 X 100 | 361.5 X 361.5 X 361.5 | $10^8 \text{ s}^{-1} / 10^9 \text{ s}^{-1}$ |
| R_2.0_BFR | 2.0 | 200 X 100 | 361.5 X 361.5 X 361.5 | $10^8 \text{ s}^{-1} / 10^9 \text{ s}^{-1}$ |
| R_2.8_BFR | 2.8 | 200 X 100 | 361.5 X 361.5 X 361.5 | $10^8 \text{ s}^{-1} / 10^9 \text{ s}^{-1}$ |
| R_2.4_9 | 2.4 | 100 X 50 | 361.5 X 361.5 X 361.5 | 10^9 s^{-1} |
| R_2.4_BZ_8 | 2.4 | 100 X 50 | 506.1 X 506.1 X 506.1 | 10^8 s^{-1} |
| R_2.4_BZ_9 | 2.4 | 100 X 50 | 506.1 X 506.1 X 506.1 | 10^9 s^{-1} |

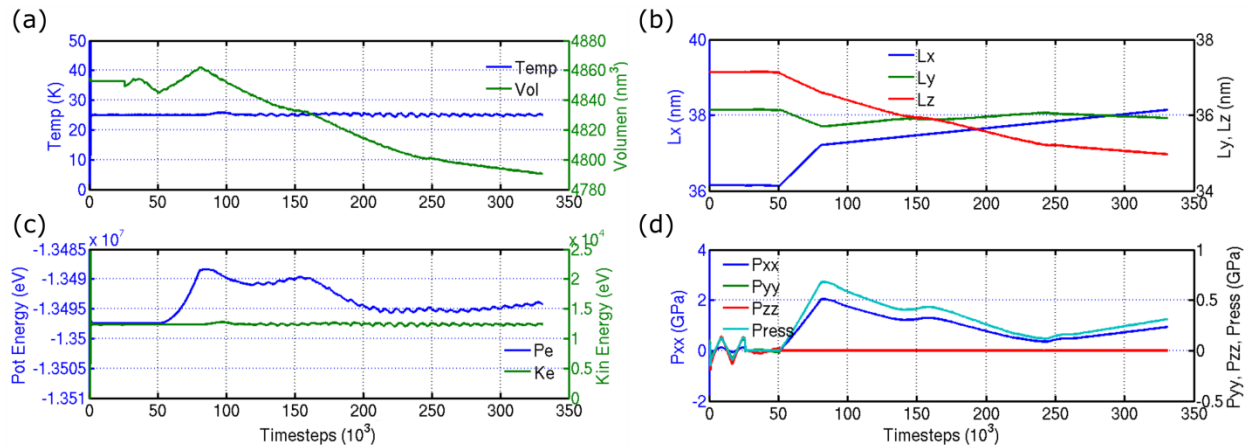


Figure 3.3: Thermodynamic control parameters during surface equilibration. (a) Temperature and Volumen vs time. (b) Dimension of the simulation box in the three direction vs time. (c) Potential and Kinetic energy vs time. (d) Pressure acting on the faces of the simulation box vs time (Press is the hydrostatic pressure of the system i.e., the trace of the stress tensor).

After the deformation take place, the evolution of L_x shows strain rate changes at 80 000 steps, at the point where the slop changes. This increase in L_x induces a reduction in L_y and L_z as a reaction of the internal force of the atoms. The pressures and volume increase according to the rate of deformation implemented until strain rate variations.

The reduction by ten times this value changes also the rate of L_z diminution and produces an increase in L_x . As consequences the pressure and the potential energy are reduced to reach equilibrium. During the complete test, the temperature keeps its value of 25 K thus the kinetic energy remains constant. The pressures on X and Z faces remain close to zero.

After the first studies (R_2.4_9, and R_2.4_BZ_9), it was observed that reforming at strain rate of 10^9 s^{-1} during the complete simulation of the system leads to high stress values (Figure 3.4a), what is not convenient to observe dislocation interactions with the RS (i.e., surface effect might be screened by the high applied stress). Taking into account the shear modulus for Cu $G=48 \text{ GPa}$, the Burgers vector $2.556 \cdot 10^{-10} \text{ m}$, the Schmid factor as $m=0.408$, it is possible to estimate the stress to open the FR source by using equation (2.19). The result of the calculations shows a value of approximately 3 GPa to open the dislocation. However, the real value observed is slightly lower. This is due to the pinning segments that starts increasing their distance reducing in that way the stress for open the initial FR dislocation. Once the dislocation is open and propagate, the stress should reduce, what is not observed in Figure 3.4a for R_2.4_9. Instead, the stress continues to increase. It occurs because the dislocation density is slow and the stress needs to increase to reach the strain rate of 10^9 s^{-1} following the Orowan equation. Once the stress reaches the value of 4 GPa, there is dislocations nucleation at the surface of the sample, the dislocation density increase and the stress decrease until reaching a steady-state. At this point, the number of dislocation is too high and counting for a dislocation density is not reasonable (or would require to code new tools). For the sample R_2.4_BZ_9, the dimension of the sample increase and the maximum stress needed to reach the strain rate imposed increase also (due to the dislocation density lowering). If we consider the velocity of dislocation expressed as $v = b\tau/B$ with $B=10^{-4} \text{ dyn s cm}^{-2}$ the viscous drag coefficient, and we mix it in equations 2.18 and 2.19 we end up with equation (3.1) what is valid for both samples. Then we can write $\frac{\tau_1}{\tau_2} = \frac{\rho_2}{\rho_1}$ with the sub index 1 and 2 referring to the samples R_2.4_9, and R_2.4_BZ_9 with mobile dislocation density of $2.1 \cdot 10^{15} \text{ m}^{-2}$ and $1.2 \cdot 10^{15} \text{ m}^{-2}$ respectively. The dislocation density was calculated considering a pair of straight dislocation that intercepts bot opposite face of the sample and moves in a 45° plane. The previous equation shows a proportionality of 0.6 between the stresses and dislocation densities what confirms that the increase in the stress is only due to a decrease in mobile dislocation density.

$$\tau = \frac{B\dot{\gamma}}{\rho b^2} \quad (3.1)$$

When the simulation is done with lower strain rate (R_2.4_BZ_8) the time needed to reach the stress value to open the dislocation is higher and takes long computational cost (result not shown). The results

showed in Figure 3.4a indicate the needs to reach the region of stable values of Stress to be capable to infer the velocity of dislocations by using Orowan model.

With this end and in order to increase computation performance, we have tested a new approach considering deformation divided into two regimes (see section 2.5 for details) and the smaller size of the samples was chosen with different b and FR sizes. In this case, for all the different samples studied, the same pattern was observed in the strain stress curve (Figure 3.4b).

The stress-strain curve shows the same pattern for the four samples tested. It is possible to identify four important events over the stress-strain curve. The first one refers to the bending of the dislocation in the linear part of the curve (marked 1 in Figure 3.4b-c).

The second critical point identified is the change of strain rate imposed (marked with number 2 in Figure 3.4b-c). It occurs at 0.03 % of deformation. It was imposed at the time that the two dislocations are already fully opened and gliding through the crystal. Once the strain rate is changed, the stress is immediately reduced. In this case, the stress is over the magnitude needed to reach the 10^8 strain rate and as a consequence the stress is reduced drastically. This confirms that the dynamic of the system is ruled by the Orowan stress and not by the stress required to open the dislocation (considering the given sample size, FR size and dislocation density).

At critical point three, the dislocation stops due to a surface step (see further discussion) and the system tend to increase the stress to make the dislocation glides again. Once it is gliding, the stress continues to reduce. For the sample R_2.4_BFR the initial dislocation size is doubled, what makes the stress to open it to be reduced in half (1.5 GPa). Independently of the size of the FR source; all the samples tend to reach the stress value around 0.5. It is because the dislocation density and the strain rate at this stage is the same for all four samples.

The final point is the minimum in the curve of Figure 3.4b. At this stage the stress increases linearly again with the same slope of the initial part. The reason why it happens is that the dislocation are moving in a periodic system in X and Y direction. They go out and reenter in the simulation cell several times until they find each other at enough short distance and they annihilate. With no dislocation present anymore within the sample the stress reincreases elastically until new dislocations are created (e.g., dislocation nucleation from surface steps). One can notice that slope of the stress increase is exactly the same than in the initial elastic regime due to the lack of dislocation. The simulation is stopped few steps after the dislocations annihilate.

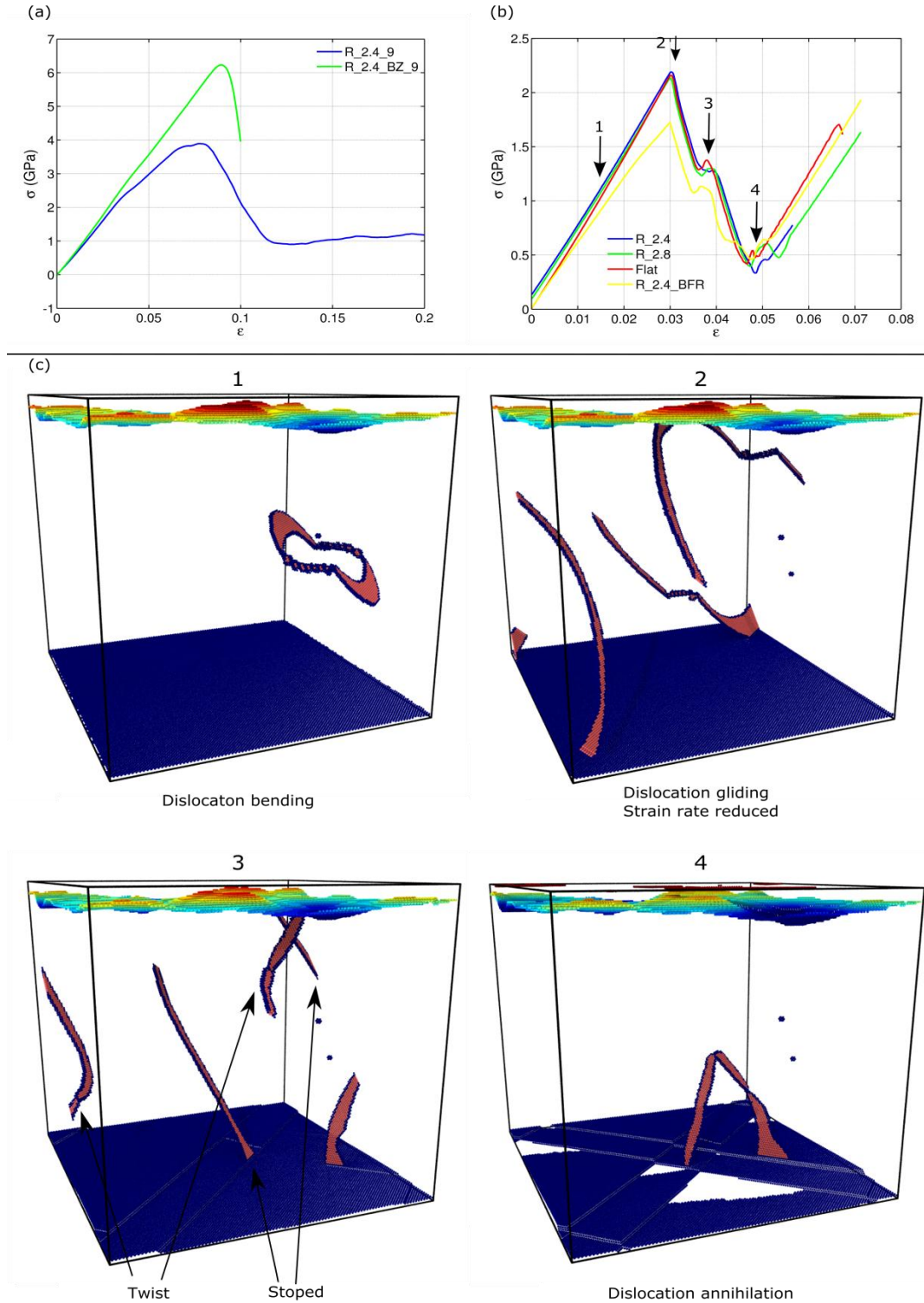


Figure 3.4: Strain-stress curve for the different samples tested under tension. (a), stress evolution of samples R_2.4_9 and R_2.4_BZ_9, (b) Stress evolution of samples with the two steps rate. The main stages are marked (1-4) (c) Status of the sample and dislocations in the stages 1-4 mentioned in the figure b.

The simulations show two behaviors (at point 3 in Figure 3.4b-c) that can be related to each other. One is the stop of dislocation when facing a surface step and the second one is the twist of the dislocation in the opposite face. Figure 3.5a shows the stop of a dislocation segment when it meets a step at the bottom of the sample that was kept perfectly flat. As a consequence, the other extreme of the dislocation reduce its velocity to 4.05 Å/ps followed by twist of its direction of propagation (Figure 3.5b).

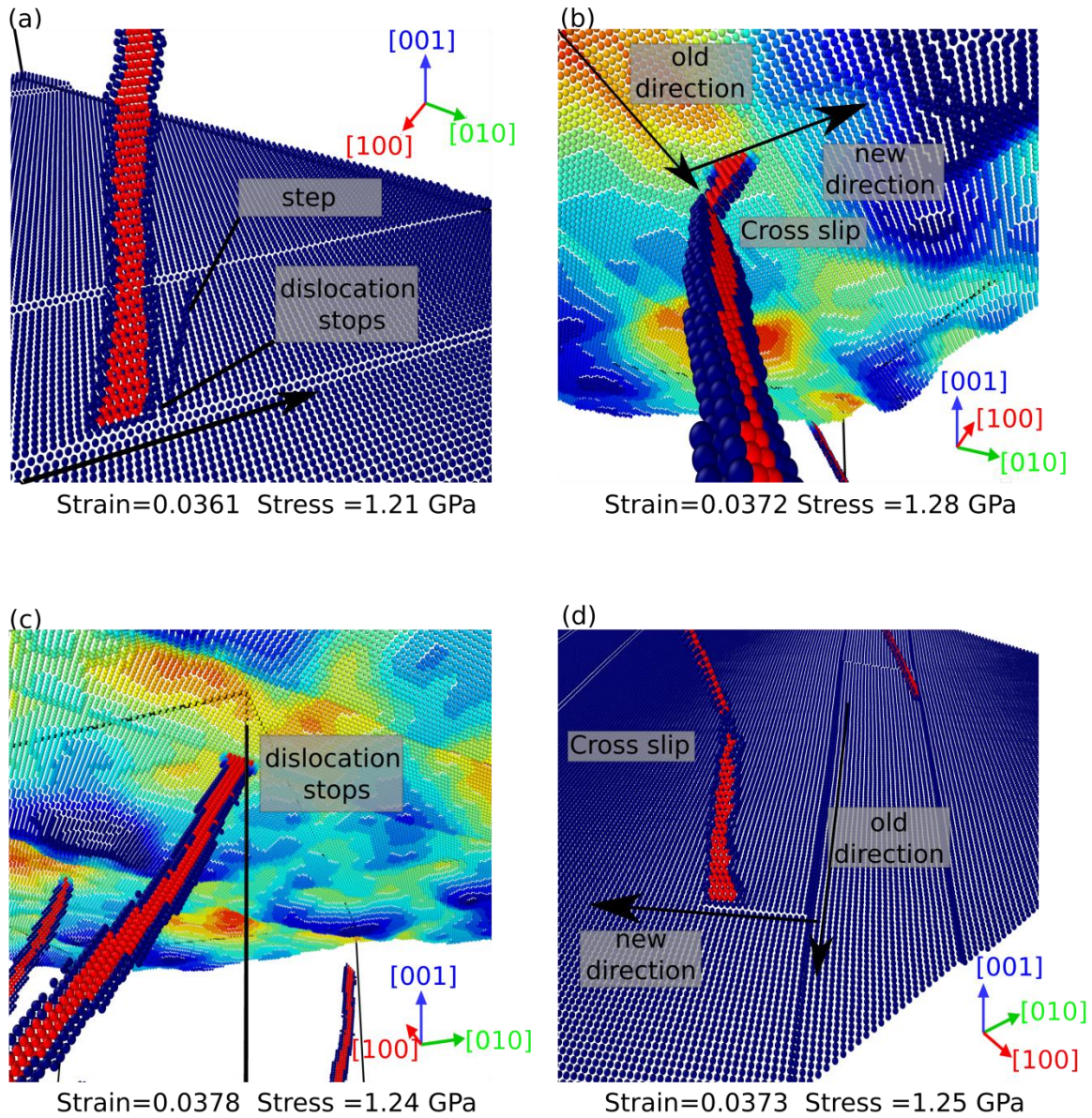


Figure 3.5: Stop and twist for two branches of the same FR dislocation. (a) 1st dislocation stopping due surface step, (b) Twist of the same dislocation at the opposite face. (c) 2nd dislocation stops at the surface. (d) Same dislocation twisted. The old and new direction of propagation is indicated with arrows.

The opposite case is also observed in Figure 3.5c-d i.e., the dislocation stops due to interaction with the step at the roughness and it induce a twist in the corresponding extreme moving in the flat surface at the bottom. This step-made are the result of the interaction of the pinning segments with the surface once the FR sources opens and glide.

The reason why this twist occurs is not completely clear, but it may be related to a minimization of the system by changing the dislocation character close to the surface. This phenomenon was also observed in a sample with perfect flat surfaces. The step responsible for stopping the dislocation is produced due to the interception of the pinning segments with the Z-surfaces. It was observed that this artifact produce a 90 degree step at the surface that may be a hard obstruction to overcome for the dislocation during its movement at low strain rate. This is a similar effect to the experimental result observed by Coupeau in Ni_3Al .

We attempt to obtain information about the change of velocity when the dislocations move through a sample with RS. We tried to perform tracking of dislocations at the surface using image processing software's like FIJI with very bad results. The dislocation is currently changing the geometrical size every time and when it happened between frames the software is not capable to recognize the same dislocation and a new one is incorporate. With these limitations is not possible to give a true value for dislocation velocity. However, the velocity was roughly extracted manually using cartography-sailing methods to only have an idea how much was the propagation velocity and its possible changes (if any).

The center of the dislocation at the surface was pointed over a printed view of the top surface and after some different frames the distance travelled was estimated using a ruler and the number of frames and time-step/number-of-frames was take into account to estimate the velocity in $\text{\AA}/\text{ps}$. In the initial part of the simulation the velocity was around $7.51 \text{ \AA}/\text{ps}$ while in the final part values of $1.2 \text{ \AA}/\text{ps}$ was observed.

The strategy used to reach the stable low stress region to estimate the velocity of the dislocation is vanished when the dislocation annihilate. New considerations may be done in order to roughly estimate any change in velocity influenced by the roughness. Especially in a deformation regime without stress in steady-state. We solved the problem of the stress regime by comparing two similar samples; Flat and R_2.4 (see table 3.1), which show same stress response (figure 3.4b). In both samples are kept the same FR source size, located in the same position and with the same orientation. Both experience the same minimization-equilibration-deformation process. The deformation includes the two stages strain rate, as we mention before. Using Ovito, the two samples were superimposed. The top surface of the flat sample was removed for clarity (Figure 3.5) and a small part of both dislocations are shown over imposed to a bottom view of the color coded roughness. There are present two pairs of brands from the same FR source. One pair starts moving from the center of the figure to the bottom-left corner while the other one moves from the center to the corner in the top-right. The dislocations with borders in purple belong to the flat sample. We call A and A' to the same brand but referring to rough and flat sample respectively. In the same way we call the second brand B and B'. The dislocations enter more than once in the simulation box due to PBC.

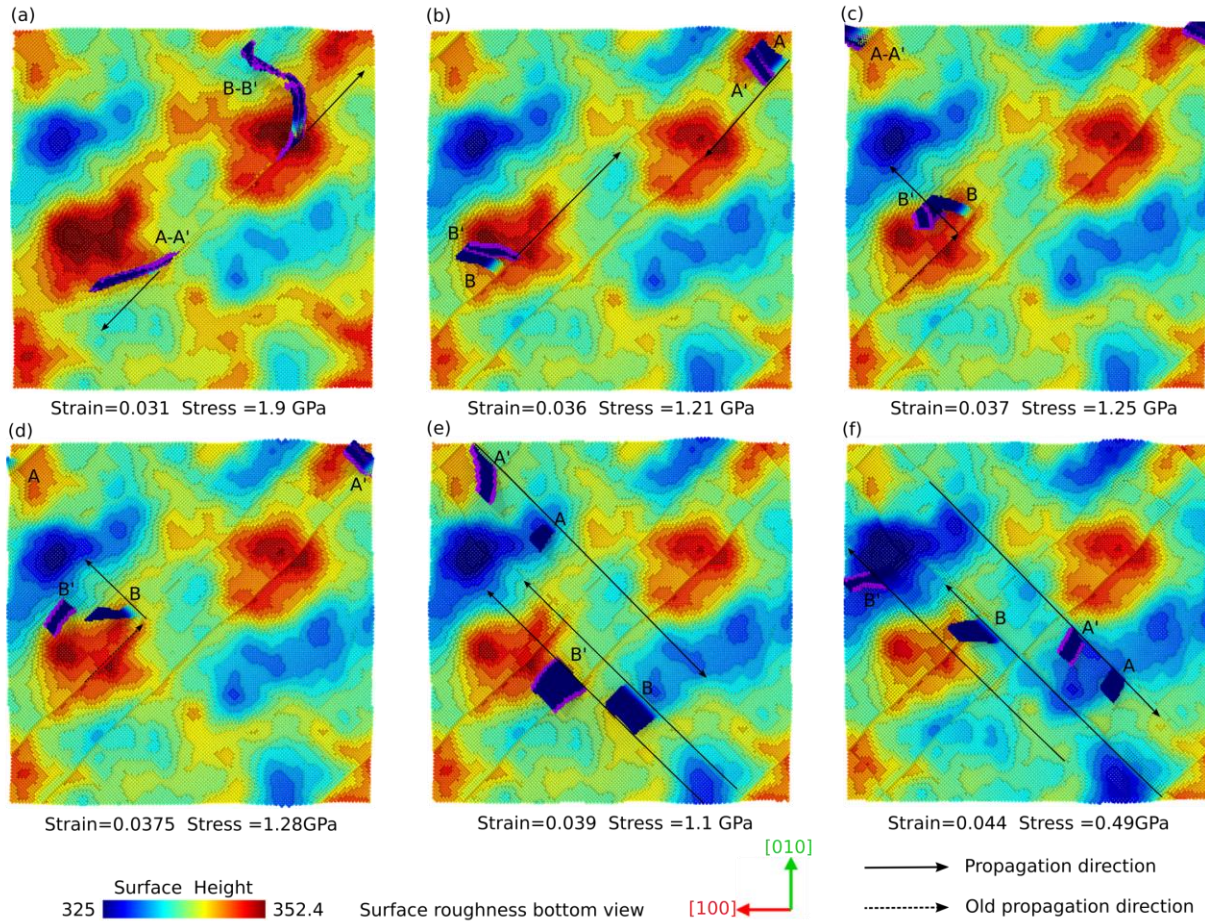


Figure 3.6: Comparison of the dislocation propagation at the surface of two samples; a “Flat” and a rough ($b=2.4$). A and B represent the two dislocations for the rough surface sample. A’ and B’ represent the same dislocations for the flat sample. All figures are taken from a bottom view. The Z-top flat surface and all FCC atoms were removed. The solid arrow represents the actual propagation direction. The dashed arrow represents the old propagation direction and their interception point is the twist occurs (a) All dislocations arriving together to the surface. (b) Light difference in position due to influence of roughness. (c-d) Different locations for twisting between rough and flat samples. (e-f) Position of the dislocations showing the influence of roughness in the velocity of propagation at the top surface.

The dislocation moves together during the initial part where the strain rate is still high (Figure 3.6a). Once the stress is reduced the dislocation start feeling the effect of roughness as we can see in Figure 3.5b. The brand AA’ re-enter in the top right corner and the A’ is located in advance of A. Same situation is observed for BB’ pairs. In this case also B’ is at the front of B with a distance a bit larger when compared to the separation between AA’ in the same frame.

Figure 3.6c shows the B’ twisted and moving in a different {111} plane while B still gliding in the previous plane. In the Figure 3.5c is possible to appreciate that dislocation B change the gliding plane later in time and position. In this case, we can interpret that B is affected by the resistance made by the roughness.

For instance, once it overcomes the higher part of the roughness colored in red. For both Figure 3.6 (c) and (d) the dislocation AA' are stop (top-corners) because of the step caused by the pinning points but their prolonged part that stills moving at the opposite bottom surface will twist and change the gliding plane (Figure 3.6d).

When the FR dislocation opens the pinning segments intercepts both surfaces up and down. It causes a one layer surface step that makes A and A' stop in Figure 3.6c-d (process explained in figure 3.5c-d). The dislocation A stops first at the pinning-step in the rough surface and because of it the twisting process starts earlier when compared with A'. Once the twist is made in both A and A' branches the A will be found at the front (Figure 3.6e), contrary to the case of BB'. When both dislocations twist they will move periodically from the bottom-right to the top-left for BB' and from the top-left to the bottom right for AA'.

By comparing the distance between A-A' and the distance between B-B' of Figure 3.5f with respect Figure3.5e is possible to notice the difference in velocity. B' looks moving farther from B while A' is seem to be "catching" A. The A' dislocation moves faster. From this analysis we can conclude that the roughness has two effects over the mobility of the dislocation. One is reducing the velocity of the dislocation (Figure3.5 b,e,f) and other is possibly influencing its slip plan by a pinning/twist process (Figure3.5 c, d).

For a better understanding of the effects mentioned before, a precise method for calculate the velocity of dislocation is needed. By using an efficient tracking dislocation method combined with a high rate of screen-shots a correlation between the dislocation velocity and the roughness could be found. Also reaching the low stress without annihilation of the dislocation will be required.

IV. CONCLUSION

In this work we introduce the principal methods used to mathematically generate random surfaces. We implemented the Sjodin [15] method for RS because of its simplicity, tunability and periodicity, what makes it perfect not only for introducing roughness in flat areas but also, for producing 3D objects with roughness at their surface by a simple coordinate transformation method that can be applied to different simulation cases.

We present an efficient methodology for introduce RS in geometrical samples that can be applicable to different mechanical simulations scenarios. We observed that the potential energy of the sample is reduced when a thermal equilibration is performed. During this process a re-accommodation of atoms takes place at the surface by diffusion. In our few simulations, it does not induce significative changes in the roughness morphology and do not affect the dislocation mobility at the strain rate, but it could still have an influence in other cases. The strain-stress curves were explained in terms of the basic linear equation of plasticity by considering the bulk material constants. It was shown that the roughness at the surface is able to reduce the velocity of dislocation and affect the position where a twist mechanism occur. Also, the simulations shows that at lower strain rate the dislocation is stopped by one layer surface step produce in the flat surface; a similar process that the one observed by Coupeau's group, in Ni_3Al .

In the future, better results could be obtained if reaching the stable lower stress regime with single pair of dislocation moving. For instance, increasing the sample and the FR dislocation size may reduce the strain rate of the simulation with the disadvantage of increase the computational cost.

References

- (1) Coppens, M. The Effect Of Fractal Surface Roughness On Diffusion And Reaction In Porous Catalysts – From Fundamentals To Practical Applications. *Catalysis Today* 1999, 53, 225-243.
- (2) Wenzel, R. Surface Roughness And Contact Angle. *The Journal of Physical and Colloid Chemistry* 1949, 53, 1466-1467.
- (3) Jiang, Y.; Li, B.; Tanabashi, Y. Estimating The Relation Between Surface Roughness And Mechanical Properties Of Rock Joints. *International Journal of Rock Mechanics and Mining Sciences* 2006, 43, 837-846.
- (4) Zhou, F.; Adachi, K.; Kato, K. Influence Of Deposition Parameters On Surface Roughness And Mechanical Properties Of Boron Carbon Nitride Coatings Synthesized By Ion Beam Assisted Deposition. *Thin Solid Films* 2006, 497, 210-217.
- (5) Kogut, L.; Komvopoulos, K. Electrical Contact Resistance Theory For Conductive Rough Surfaces. *Journal of Applied Physics* 2003, 94, 3153-3162.
- (6) Palanchoke, U.; Jovanov, V.; Kurz, H.; Dewan, R.; Magnus, P.; Stiebig, H.; Knipp, D. Influence Of Back Contact Roughness On Light Trapping And Plasmonic Losses Of Randomly Textured Amorphous Silicon Thin Film Solar Cells. *Applied Physics Letters* 2013, 102, 083501.
- (7) Nahas, Y.; Berneau, F.; Bonneville, J.; Coupeau, C.; Drouet, M.; Lamongie, B.; Marteau, M.; Michel, J.; Tanguy, P.; Tromas, C. An experimental UHV AFM-STM device for characterizing surface nanostructures under stress/strain at variable temperature (accessed Sep 2, 2018).
- (8) Coupeau, C.; Camara, O.; Drouet, M.; Durinck, J.; Bonneville, J.; Colin, J.; Grilhé, J. Slip-Trace-Induced Vicinal Step Destabilization. *Physical Review B* 2016, 93.
- (9) Veyssi re, P.; Yoo, M.; Horton, J.; Liu, C. Temperature Effect On Superdislocation Dissociation On A Cube Plane In Ni3Al. *Philosophical Magazine Letters* 1989, 59, 61-68.
- (10) Pastewka, L.; Robbins, M. Contact Between Rough Surfaces And A Criterion For Macroscopic Adhesion. *Proceedings of the National Academy of Sciences* 2014, 111, 3298-3303.
- (11) Ramisetti, S.; Campa  a, C.; Anciaux, G.; Molinari, J.; M user, M.; Robbins, M. The Autocorrelation Function For Island Areas On Self-Affine Surfaces. *Journal of Physics: Condensed Matter* 2011, 23, 215004.
- (12) Patir, N. A Numerical Procedure For Random Generation Of Rough Surfaces. *Wear* 1978, 47, 263-277.
- (13) Hu, Y.; Tonder, K. Simulation Of 3-D Random Rough Surface By 2-D Digital Filter And Fourier Analysis. *International Journal of Machine Tools and Manufacture* 1992, 32, 83-90.
- (14) Watson, W.; King, T.; Spedding, T.; Stout, K. The Machined Surface — Time Series Modelling. *Wear* 1979, 57, 195-205.

- (15) Sjodin, B. How to Generate Random Surfaces in COMSOL Multiphysics® <https://www.comsol.com/blogs/how-to-generate-random-surfaces-in-comsol-multiphysics/> (accessed Jul 9, 2017).
- (16) de Koning, M.; Cai, W.; Bulatov, V. Anomalous Dislocation Multiplication In FCC Metals. *Physical Review Letters* 2003, *91*.
- (17) Plimpton, S. Fast Parallel Algorithms For Short-Range Molecular Dynamics. *Journal of Computational Physics* 1995, *117*, 1-19.
- (18) Mishin, Y.; Mehl, M.; Papaconstantopoulos, D.; Voter, A.; Kress, J. Structural Stability And Lattice Defects In Copper:Ab Initio, Tight-Binding, And Embedded-Atom Calculations. *Physical Review B* 2001, *63*.
- (19) Hirel, P. AtomsK: A Tool For Manipulating And Converting Atomic Data Files. *Computer Physics Communications* 2015, *197*, 212-219.
- (20) Stukowski, A. Visualization And Analysis Of Atomistic Simulation Data With OVITO—The Open Visualization Tool. *Modelling and Simulation in Materials Science and Engineering* 2009, *18*, 015012.
- (21) Bakolas, V. Numerical Generation Of Arbitrarily Oriented Non-Gaussian Three-Dimensional Rough Surfaces. *Wear* 2003, *254*, 546-554
- (22) Fang, T.; Chang, W. Effects Of AFM-Based Nanomachining Process On Aluminum Surface. *Journal of Physics and Chemistry of Solids* 2003, *64*, 913-918
- (23) Petrik, P.; Biró, L.; Fried, M.; Lohner, T.; Berger, R.; Schneider, C.; Gyulai, J.; Ryssel, H. Comparative Study Of Surface Roughness Measured On Polysilicon Using Spectroscopic Ellipsometry And Atomic Force Microscopy. *Thin Solid Films* 1998, *315*, 186-191.
- (24) Nose, S. A Molecular Dynamic Method For Simulations In The Canonical Ensemble. *Molecular Physics* 1984, *52*, 2, 255-268.